

Shallow granular flows down flat frictional channels: steady flows and longitudinal vortices.

Nicolas Brodu, Patrick Richard, and Renaud Delannay

Institut Physique de Rennes, UMR CNRS 6251,

Université de Rennes 1, Campus de Beaulieu Bâtiment 11A,

263 av. Général Leclerc, 35042 Rennes CEDEX

Granular flows down inclined channels with smooth boundaries are common in nature and industry. Nevertheless, flat boundaries have been much less investigated than bumpy ones, which are used by most experimental and numerical studies to avoid sliding effects. Using DEM numerical simulations with side walls we recover quantitatively experimental results. At larger angles we predict a rich behavior, including granular convection and inverted density profiles suggesting a Rayleigh-Bénard type of instability. In many aspects flows on a flat base can be seen as flows over an effective bumpy base made of the basal rolling layer, giving Bagnold-type profiles in the overburden. We have tested a simple viscoplastic rheological model (Nature 2006, vol 441, pp727-730) in average form. The transition between the unidirectional and the convective flows is then clearly apparent as a discontinuity in the constitutive relation.

PACS numbers: 47.57.Gc, 45.70.-n

I. INTRODUCTION

Granular dense flows down inclined channels preserve the complexity of granular flows while remaining simple enough for a detailed analysis [1]. They are of interest in engineering applications involving conveying of solid materials such as minerals, or in geophysical situations like rock avalanches or pyroclastic flows. This article focuses on flows down a flat, frictional incline. These flows differ substantially from those on a rough or bumpy base with macroscopic asperities on the order of the diameter of the flowing particles. We have developed simulations that model the experimental configuration used by Louge and Keast [2]: shallow flows (≈ 7 grain diameters at rest height, see Fig. 4) in a wide (≈ 68 grains) chute with flat frictional surfaces. We investigate flows in a range of inclination angles containing the range of experimentally observed Steady and Fully Developed (SFD) flows. We reproduce the flow properties quantitatively and analyze the internal flow structure. We show that above a given inclination angle granular convection occurs in association with inverted density profiles. To our best knowledge our work is the first to predict that secondary flows also exist with flat boundaries for SFD flows. The basal rolling layer can be seen as an effective “bumpy” base for the core flow sliding on top of it [1, 3]. In these conditions, we show that velocities in the main bulk of the flow follow a Bagnold scaling. This type of flows is associated with a constant homogeneous inertial number for SFD flows on a bumpy base [4]. This led us to study the rheology of these flows, and test whether the viscoplastic rheology holds.

The paper is structured as follows. The next section, which can be skipped by specialists of the field, is devoted to the state of the art. Section 3 gives details about the simulation method we will use. Global properties of the flows are studied in section 4. Section 5 is devoted to de-

tailed results concerning the packing fraction, pressure, velocity and “granular temperature” fields. The rheological study is presented in Section 6. Concluding remarks are given in Section 7.

II. THE STATE OF THE ART ON GRANULAR FLOWS DOWN INCLINED CHANNELS

Significant progress have been made during the last decades in describing dense granular flows, nevertheless they continue to resist our understanding and remain an active field of research. Very dense quasistatic regimes are usually described by plastic models [5], and a kinetic theory of granular gas has been developed [6] that can accurately render the behavior of dilute flows. A viscoplastic description for dense fluid regimes has been proposed based on a dimensionality analysis in the unidirectional case [4]. This rheology has then been extended to 3D for incompressible flows [7]. In all these cases, when the parameters are set according to the expected theoretical values (e.g. high packing fraction dense uniform flows, initial and boundary conditions, etc.), the proposed constitutive equations match the experiment (e.g. collapse of velocity profiles [8]). Extensions are then proposed to account for variations of nearly related cases: an extended granular gas theory taking into account correlations in denser cases [9], or a variant of the viscoplastic model for compressible flows [10]. Despite all these efforts, a comprehensive theory is still missing in the general and most common case where the coexistence of both dense and dilute parts are observed within the same flow, and which would correctly incorporate the influence of boundary conditions such as sidewalls and bottom.

A large corpus of studies exists on dense granular flows down an inclined plane chute (more than 100 references in [4], additional ones in [1]). The boundaries are known to change the flow structure [11]. The choice of wide

channels is an attempt to avoid the influence of sidewalls. In the same way, numerical simulations in periodic cells attempt to study flows down infinitely long and wide chutes. Most experimental and numerical works avoid the inherent discontinuity and sliding at the base by covering the surface with glued, fixed grains of the same nature as those involved in the flow [8, 11–13]. In these conditions there exist limits on the lower inclination angle and the piling height below which the grains do not flow. Above these thresholds and for moderate inclinations, dense fluid flows present a negligible velocity at the bumpy base. Thin SFD flows comprising a few layers of grains exhibit a nearly linear, sheared vertical profile of the velocity ([4], 2D experiments [14–16], 2D [17] and 3D periodic [12] numerical simulations). For thicker flows, a Bagnold scaling is observed in the core of the SFD flow, with lower velocities at the base ([4], 3D periodic numerical simulations [12]). At larger angles of inclination the flows are more dilute and an inverted density profile is observed [10, 18, 19]. This inversion was analyzed by means of the granular gas theory to induce a Rayleigh-Bénard type of instability [13, 19]. The convection rolls take the form of longitudinal stripe patterns [10, 13]. These can be reproduced numerically using Periodic Boundary Conditions (PBC) [10] provided the width the periodic cell, W , is large enough compared to the grain diameter D for the convection rolls to appear. Convection has never been observed in numerical works using $W = 10D$ [12, 20]. Below about $W \approx 50D$, there seems to be not enough space for developing convection rolls [10].

Beside these studies of “unconfined” flows in large channels, extensive measurements highlighting the influence of walls were performed [21–24]. Experimental and numerical studies both in 2D and 3D configurations [23] show that frictional lateral walls alter the flow properties. For instance, SFD flows on bumpy bases are observed up to large inclination angles where accelerated ones are usually expected. Moreover, at any given inclination angle, there is a critical flow rate above which a static heap forms along the base. The heap is stabilized by the flow atop it [22]. Flows atop this sidewall-stabilized heap (SSH) differ from SFD flows on bumpy base as they occur over erodible bases, but still display SFD features. The effect of side walls on SFD flows on top of a static pile in a channel has been studied by carrying out experiments in setup of different widths, up to 600 particle diameters [24]. They show that these flows are entirely controlled by side wall effects.

The bumpy bases made of glued grains case is thus relatively well-studied. However most industrial conditions involve flat boundaries, as well as natural flows occurring on smooth bed rocks at the scale of the grains. Surprisingly very few studies [2, 11, 25–32] have considered this more common case of flat frictional surfaces. Early experimental works mention increased flow velocity and sliding conditions at the boundaries compared to the bumpy walls case [11]. Differences with the bumpy case situation are manifest in the flow properties. Velocity profiles

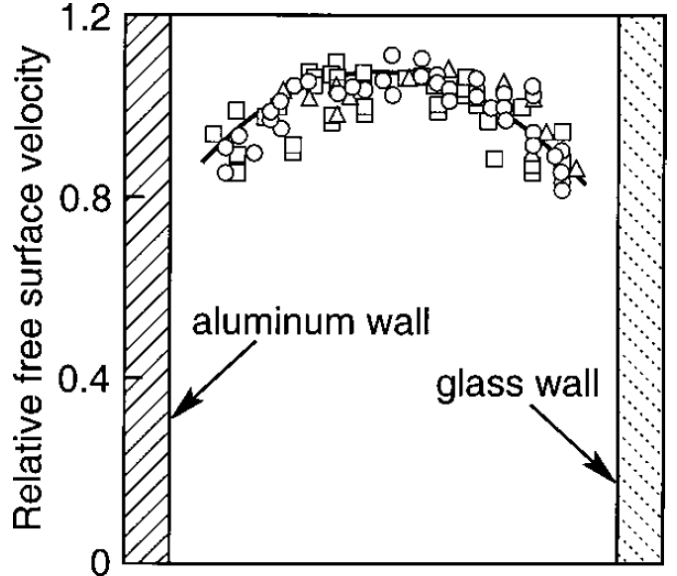


Figure 1. Top view of free surface velocity profiles for granular flows down flat and frictional base (reprinted from [2]). The influence of the side walls is apparent over 2/3 of the flow width.

(transversal and in height) involve a slip condition at the boundaries [29], compared to the null velocity condition at the interface with the bumpy walls. Some unexplained surging waves are occasionally observed at the surface [2, 11], blurring its exact location by a layer of grains in saltation. More recently Louge and Keast [2] conducted experiments on a flat base with a well documented set of parameters, with a more detailed analysis than previous experimental works on the topic [27–30]. They confirmed the aforementioned observations regarding the flow structure and velocity profiles. A layer of rolling grains with intermittent jumps develops on the flat base, with the rest of the flow sliding on top of this basal layer. The influence of the distant side-walls is negligible in terms of induced friction: “the relative contribution of side walls in the force balance [...] never exceeds 7%” [2]. However this influence of the side walls is clearly apparent over 2/3 of the flow width (Fig. 1), reprinted from [2]), leading to the conclusion that some other mechanism is involved for a long-range influence of the boundary conditions.

They also reported a range of inclination angles $[\theta_{\min}, \theta_{\max}]$ for the observation of steady fully developed (SFD) flows, independent of the flow height, that presents a much lower bound than in the bumpy surface case [8]. The upper bound for SFD flows is also provided, but as correctly pointed out by [33] the attainment of SFD flows is restricted by the physical length of the chute, hence so is the maximal angle above which an “accelerated regime” is observed. Numerical simulations can be used in order to complement these experimental results, but literature on numerical studies over flat frictional surfaces is sparse. Early simulations are reported in [25] (2D) and [31] (3D). Given their limited computa-

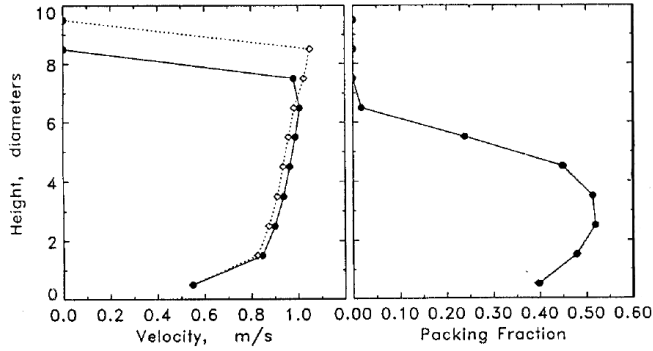


Figure 2. . Velocity (left) and packing fraction (right) profiles obtained by Walton [31] for moderate flow heights. Solid lines are instantaneous profiles, dotted line is time average profiles. Reprinted from [31].

tional power, implying the use of a small periodic cell and a low number of grains, and given their use of monodisperse grains, a direct comparison with the experiment is difficult. More recent numerical works considering a flat base [3] do not provide a detailed analysis of its influence. Without sidewalls SFD flows on a flat base can only be sustained for inclination angles whose tangent is less than the friction coefficient [2, 31]. Thus, with PBC, the maximal inclination angle θ_{\max} is fixed by the solid friction on the base: $\mu = \tan \theta_{\max}$. Walton [31] got effectively SFD flows for inclination angles θ whose tangent is smaller than the friction coefficient μ , else they accelerate unboundedly. Nevertheless the experimental value of θ_{\max} lead to choosing a large value of μ which is not compatible with the friction coefficients measured in impacts [2, 34]. The value of the lower bound θ_{\min} is not available in [31]. Velocity profiles as a function of distance from base at low angle in [31] show a seemingly linear shearing in the bulk region (above the rolling layer - see Fig. 2) for thin flows, which turn into constant-velocity crystallized plugs at larger thickness.

At larger angles but in 2D [25], the profiles of the packing fraction, the velocity and its fluctuations, are of the same type as these predicted by kinetic theories (type II in [30]), with an inversion of the density profile and a higher “granular temperature” at the base than at the surface. The state of art on granular flows down flat frictional channels thus remain largely incomplete, with limited numerical simulations not able to complement and detail the inner details of the flows reported in experimental works.

III. SIMULATION METHOD

We perform 3D numerical simulations of granular flows using molecular dynamics (MD) that consist in integrating the equations of motion over time. Each grain is represented by a sphere whose diameter is drawn from a uniform distribution around the mean value D . The

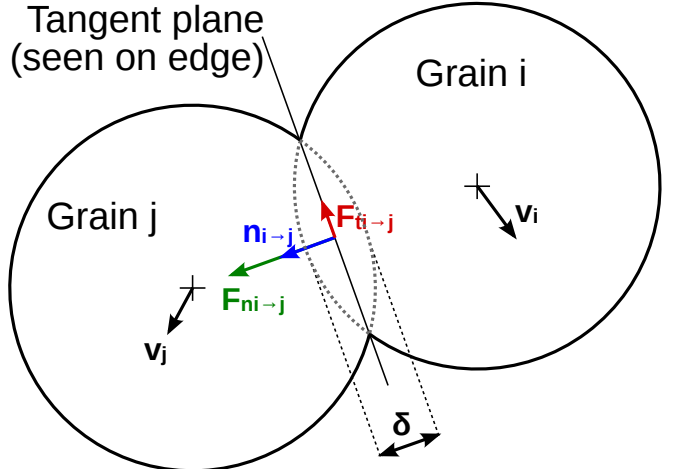


Figure 3. (Color online). Overlapping spheres contact model. Grain i moves with a translation velocity v_i , and similarly for j . The force exerted by grain i on grain j during contact (characterized by the normal vector $n^{i \rightarrow j}$) is decomposed into a tangential component $F_t^{i \rightarrow j}$ and a normal component $F_n^{i \rightarrow j}$. Both depend on the overlap δ according to a contact model detailed in the main text.

grain model consists of a non-deformable sphere [35] of uniform material with density ρ . Deformations are taken into account by the contact model, which links the normal force \mathbf{F}_n acting on each grain to the overlap δ that occurs between the non-deformed spheres when the grains centers are closer than their diameters would allow (Fig. 3). The linear visco-elastic approach [36] is used: $\mathbf{F}_n^{i \rightarrow j} = (k_n \delta + \gamma_n v_n) \mathbf{n}^{i \rightarrow j}$, with $\mathbf{n}^{i \rightarrow j}$ the contact normal (unit vector from sphere centers i to j), $v_n = (\mathbf{v}_i - \mathbf{v}_j) \cdot \mathbf{n}^{i \rightarrow j}$ the normal component of the relative translational grain velocities, k_n a model spring stiffness and γ_n a model viscosity (i.e. giving a linear velocity-dependent force). A similar model is applied in the tangential direction: $\mathbf{F}_t^{i \rightarrow j} = (k_t s + \gamma_t v_t) \mathbf{t}^{i \rightarrow j}$, with $v_t \mathbf{t}^{i \rightarrow j} = (\mathbf{v}_i - \mathbf{v}_j) - v_n \mathbf{n}^{i \rightarrow j}$ the tangential component (i.e. with some direction within the tangential plane) of the impact velocity, k_t and γ_t a model spring stiffness and a model viscosity, and s is a bounded version $|s| \leq |\mathbf{F}_t| / k_t$ of the sliding displacement $\int_{\tau_0}^{\tau} v_t d\tau$ in the tangential plane since contact time τ_0 [37]. Coulomb friction $|\mathbf{F}_t| \leq \mu |\mathbf{F}_n|$ is enforced on the tangential component, with a model coefficient μ . Below that threshold the value of \mathbf{F}_t is given by the above equations. The torque acting on a grain is computed as $\mathbf{q} = -r (\mathbf{F}_t \times \mathbf{n})$ with r the grain radius. Both force and torque are used for integrating the equation of motions $\sum \mathbf{F} = m \mathbf{a}$ and $\sum \mathbf{q} = I \boldsymbol{\omega}$ with m the mass of a grain, \mathbf{a} its acceleration, I its moment of inertia, and $\boldsymbol{\omega}$ its angular velocity vector. Numerical integration is performed using the Velocity-Verlet scheme. This whole approach is repeated for grain-wall interactions with a different set of parameters $k_n^{gw}, k_t^{gw}, \gamma_n^{gw}, \gamma_t^{gw}, \mu^{gw}$.

Solid mechanics induces relations between these model

Grain diameter	$D = 2.968 \text{ (mm)}$
Grain mass (glass density ρ_g)	$m = 3.42 \cdot 10^{-5} \text{ (kg)}$
Gravity	$g = 9.81 \text{ (m/s}^2\text{)}$
Grain/grain normal restitution	$e_n^{gg} = 0.972$
Grain/grain tangential restitution	$e_t^{gg} = 0.25$
Grain/wall normal restitution	$e_n^{gw} = 0.8$
Grain/wall tangential restitution	$e_t^{gw} = 0.35$
Grain(glass)/grain friction	$\mu^{gg} = 0.33$
Grain(glass)/wall(aluminum)	$\mu^{gw} = 0.596$
Grain/grain spring stiffness	$k_n^{gg} = 2 \cdot 10^5 \text{ (mg/D)}$
Grain/wall $k_n^{gw} = k_n^{gg}$ (glass Young modulus = aluminum)	
Integration time step	$dt = 10^{-4} (\sqrt{gD})$

Table I. Simulation parameters matching the experimental values from [2].

parameters. For a normal collision between two grains the damped harmonic oscillator defined by the above interaction model leads to a contact duration τ_c during which $\delta > 0$ (half of the first pseudo-period). Normal relative velocities before and after contact are then related by a constant coefficient of normal restitution e_n that sets γ_n . Similarly the tangential spring/dashpot model defines a coefficient of restitution e_t . Equating both duration times leads to a relation $7k_t(\pi^2 + (\ln e_n)^2) = 2k_n(\pi^2 + (\ln e_t)^2)$, which corrects the $7k_t = 2k_n$ relation from [12] when $e_n \neq e_t$. Thanks to these relations the simulation parameters can be concisely given in Table I.

The correspondence of these parameters to physical values is subject to a few simplifications. The most drastic one is the use of a single model friction coefficient μ for all cases of static, kinetic and collisional frictions. We had to use the static friction coefficient instead of the other ones – as usually done in MD simulations [10, 12] – in order to reproduce experimental values. Hypothesis for this model/experiment discrepancy given in the literature are the presence of long lasting contacts [2] or the use of the visco-elastic contact model itself [38]. Even then, the static friction coefficient is known to be quite sensitive to the surface properties and its determination is itself a topic of debate. We used $\mu^{gg} = 0.33$ as measured in our lab between spent glass beads. Lorenz et al. [34] had to erode grains by circulating them in their experimental facilities for two hours before their results became reproducible. We used the value they give $\mu^{gw} = 0.596$ for the grain/wall contacts in our simulations, together with all their normal and tangential restitution measurements (see Table I). These restitution coefficients could be refined for binary collisions using precise velocity-dependent measures fitted by more complicated models [37], but this would not necessarily give better global results given the multiple- and long-lasting- contacts [37], so we stick to the experimental values given by [2, 34]. Similarly the use of a more complicated non-linear contact laws (e.g. Hertz) has been proposed but was found

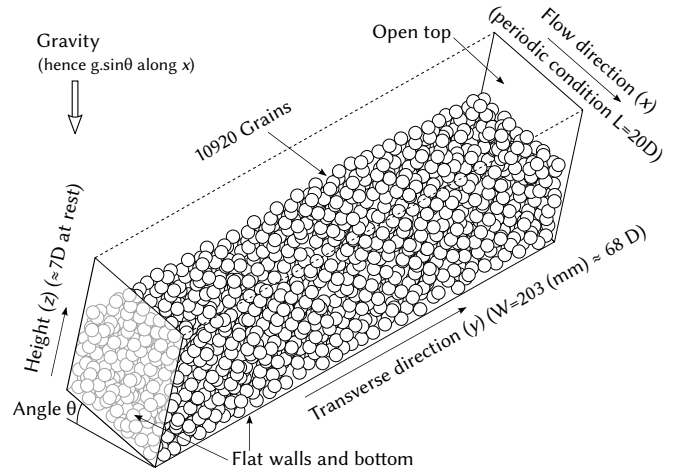


Figure 4. Sketch of the MD simulation in a configuration corresponding to experiments [2] where an inclined plane is bounded by flat side walls and base.

to be no better than a linear model on a global scale [39]. The value of the spring stiffness shall however be related to material properties. A link to the Young modulus and Poisson ratio is possible for Hertzian contacts [40]. For linear models we had to rely on an ad-hoc approximation [41] that leads to $k_n = 3 \cdot 10^5 \text{ N/m} = 3.35 \cdot 10^6 \text{ mg/D}$ (comparable to $k^n = 2.10^5 \text{ N/m}$ in [33]). In any case we checked that our results are not sensitive to the choice of k_n provided it is given a sufficiently high value, so we then used the more classical value $k_n = 2.10^5 \text{ mg/D}$ for faster simulations [12].

IV. FLOW CONFIGURATION

A. General setup

The simulation setup is designed to model the experimental setup of Louge and Keast [2], with minor adaptations (Fig. 4). The calculational space is bounded on the base and on the side walls by fixed flat frictional planes, and it is free on the top surface (see Fig. 4). PBC are applied in the flow (x) direction as we cannot simulate the whole system with current computational facilities (we use a period of $L = 20D$, similar to [12]). Initial conditions model the dropping of a loose assembly of agitated grains at a small altitude. These low energy conditions are combined with a mass holdup $\tilde{H} = 4$ compatible with the experimental configurations for all SFD flows in [2] (the mass holdup $\tilde{H} = \int_0^{+\infty} \frac{\nu(z)}{D} dz$ quantifies the amount of matter above a unit surface, with ν the volume fraction).

Preliminary simulations using PBC along y and a small periodic cell size were first performed and were able to recover the results of Walton [31]. However, the range of angles of inclination for which steady and fully developed flows are reached does not match the experimental

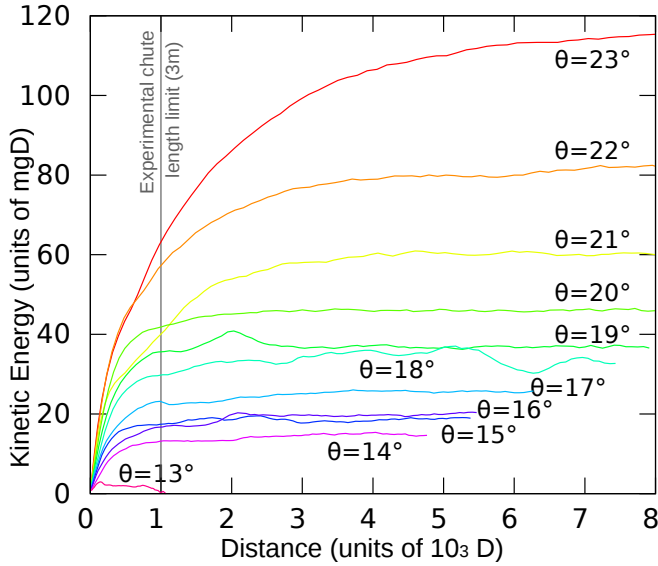


Figure 5. (Color online). Translation kinetic energy vs distance traveled by the grains, showing regimes that appear accelerated within the chute length experimental limit, but reaching steady states at larger distances.

results of Louge and Keast [2]. For example, in simulations we obtain $\theta_{\min} \approx 6 - 7^\circ$, which is much lower than the experimental value (15.5°). Neither a modification of the material parameters such as the friction and the restitution coefficients, the polydispersity of grains, nor the introduction of other sources of dissipation like rolling friction [36] gives values of θ_{\min} close the experimental one. On the contrary, the introduction of side walls separated by a gap W with identical material properties as the base is able to increase θ_{\min} to $\theta_{\min} = 14^\circ$, reasonably close to the experimental value (15.5°). Note also that, the use of the low polydispersity value given in [2] ($\pm 0.7\%$ of the average grain diameter) leads to crystallized blocks in the flow. Due to the periodicity in x these blocks tend to persist for a long time. Experimentally the grains are re-circulated and this corresponds to averaging over multiple realizations making the presence of blocks inappropriate. One way to get rid of these artifacts was to increase the polydispersity, up to 10% for all the results presented below.

B. The flow regimes

We ran simulations for a range of angles from 13° to 23° containing the range of experimentally observed SFD flows [2]. Visual investigation of the simulations shows that the main bulk of the flows rests on top of a basal layer of grains, for which there is a combination of long-lasting rolling contacts with the flat base that are interrupted by short rebounds. Fig. 5 presents the evolution of the kinetic energies of the flows over the average distance traveled by the grains. Louge and Keast [2] ex-

perimentally observed a range of angles for steady states from 15.5° to 20° , established over distances less than 3m. This matches our finding (see the vertical line in Fig. 5) that flows at higher angles would indeed appear accelerated within the experimental limits. The flows stop below $\theta_{\min} = 14^\circ$ which reasonably matches the experimental value (15.5°) as there are extra factors not taken into account in the simulation, like the abundant interparticle dust that was reported experimentally [2, 34], which might then block the flow at low velocities. The effect of the side walls on θ_{\min} mentioned by Louge and Keast [2] cannot be attributed only to additional friction, which is negligible given the shallow flow height and the large distance between the walls as aforementioned and noted in [2]. Some unknown mechanism is thus at work, which will be the topic of further studies.

Simulations with sidewalls lead to SFD flows except, maybe, for $\theta \approx 18^\circ (\pm 1^\circ)$ where relatively large fluctuations are visible on the kinetic energy in Fig. 5. These fluctuations, which persist over time (we checked it up to a distance of $\approx 13500D$), were also reported experimentally in [2], although it is not easy to determine whether these match our simulations results: the periodic size we use in x is a fraction of the oscillation wavelength observed experimentally. Hanes and Walton [33], who use a bumpy base for their experiments, also report a phase diagram with an oscillating regime delimited by fuzzy boundaries, at the junction of two SFD regimes, with the same PBC numerical interpretation difficulty. These oscillations take place at the transition between two SFD regimes which have very different behaviors. For $\theta \in [14^\circ, 17^\circ]$ flows are unidirectional and grains from ordered layers. These are visible in Fig. 6 as regions of higher packing fraction, as well as in Fig. 7a. The free surface of the flow (Fig. 7a) is convex, higher in the center than on the borders. For θ larger than 19° , secondary flows develop (Fig. 17), breaking the layer structure (Fig. 6), except for the basal layer of rolling grains (Fig. 7b). The free surface is concave (Fig. 7b). The flow height is enlarged, with a correspondingly lower average density, but the flow remains shallow (height $\approx 10D$ for a width of $68D$). The rolls are thus quite flat. Secondary flows have only been observed in experiments within a bumpy channel, *e.g.* [11] (using $D = 0.5\text{mm}$ beads) and [10] ($D = 0.4\text{mm}$). The stationary state in [11] was however reached at a distance compatible with our results, scaled by the difference in D : less than 3m at $\theta = 23.6^\circ$.

In order to quantify the effect of the geometry of the base, we have carried out the same simulations with a bumpy base consisting of fixed grains and otherwise the same parameters (including flat frictional lateral walls). In these conditions the grains flow only above 22° , with an average kinetic energy of $\approx 1mgD$. Compared to the kinetic energy $\approx 100mgD$ in Fig. 5 at the same angles, and given the much lower θ_{\min} bound in the flat case, we immediately see that no direct comparison is possible between the flat frictional base and the bumpy one: the basal layer of rolling grains significantly reduces the

dissipation. Experimentally [11] also noted a much increased flow velocity on flat surfaces. For $\theta \geq 22^\circ$ fixing grains on the base prevents the rolls but induce a large internal agitation instead. This is consistent with the results of Börzsönyi *et al.* [10] which report rolls only for thicker flows compared to our shallow flow configuration. Therefore, the convection regime is accessible for smaller systems with a flat frictional bottom than with a bumpy one.

C. Influence of the parameters and of the initial conditions

To study the generality of the above reported results we carry out an extensive study of the effect of the model parameters and of the initial conditions which is summarized below.

The transitions between the regimes and their characteristics depend slightly on the model parameters (*e.g.* friction coefficients, polydispersity of the grains) but the general features of the flows seem robust. For instance, additional runs with $\mu_{gg} = 0.4$ instead of 0.33 shifted the start and end of the unidirectional flows up by 1° . The rolls are robust to polydispersity (tested with $D \pm 20\%$). They also appear when $\mu_{gg} = \mu_{gw}$ (customary setting in numerical works [12]), provided both are greater than about 0.54.

The initial conditions we use consist of dropping a loose assembly of grains at $z = 2D$ with a low initial velocity and some jitter, which we designed to be approximately what the grains would have experimentally when leaving the open gate in [2]. The corresponding initial energy is much lower than that reached in steady state (see Fig. 5). We checked the final SFD states are robust to variations of the initial conditions provided these induce an initial energy smaller than the energy of the final SFD state. However we have not studied the use of larger energies, as we suspect there may be hysteresis effects on the final energy levels. Literature for the bumpy base case also reports [18] that specific regimes exist with high initial energy conditions, so presumably this might be a possibility for the flat frictional base case as well.

We varied the mass holdup so as to match the range of shallow flow configurations in [2]: low $\tilde{H} = 1$ induces an early transition to a dilute phase without secondary flows. Convection rolls appear between $\tilde{H} = 3$ and $\tilde{H} = 4$. They persist even for much higher mass holdups (tested up to $\tilde{H} = 20$).

The existence of a minimal angle θ_{\min} for SFD flows requires the presence of enough layers of grains, as the rolling basal layer may accelerate indefinitely with insufficient frustrations on the grain rotations (the limit case being a single grain rolling on an flat inclined plane). The investigation of the parameters and initial conditions mentioned above shows that the properties of the flows are robust. Therefore, the simulations reported here are qualitatively representative of many others obtained with

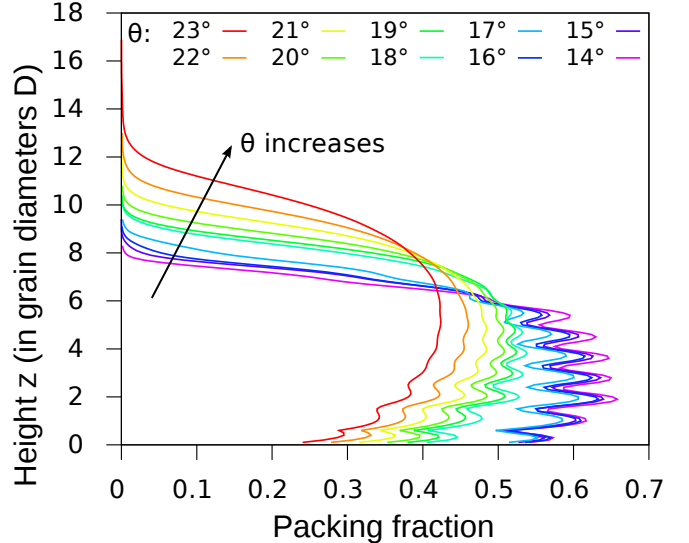


Figure 6. (Color online). Height-averaged packing fraction (smoothed over $\pm 0.5D$ in z) for each angle of inclination. The layering is clearly apparent at low angles, and disappears in the presence of the secondary flows.

different conditions.

V. STEADY STATES

This section analyzes the main features of the two families of SFD states : unidirectional and layered flows, and flows with granular convection. All the figures presented below report time averaged quantities (*e.g.* velocity, packing fraction) computed over $500 \sqrt{D/g}$ time units in steady state, as well as over the periodic cell in the flow direction. These results are stable with respect to the particular random seed we use between different runs.

A. Packing fraction

Values of the packing fraction at the base of the flow (Fig. 6) are compatible with the experiments (see for example Fig. 6 of [2], $\theta = 16^\circ, 18^\circ, 20^\circ$ and $\tilde{H} = 4$). For the unidirectional flows Fig. 6 shows that the average volume fraction $\nu \approx 0.59$ does not vary much in z above the basal layer, with clear variations around that average at each structured layer. The structuration in layers of constant packing fraction (above the basal layer) was observed by the previous numerical study [31] with PBC along y . We confirm that structure persists with a polydispersity of 10%, that it was not an artifact of the use of single-sized spheres in [31]. Another difference with [31] is the presence of 2 lateral layers (Fig. 7) at the wall boundaries, inducing some nearby structuration.

In the convective regime we observe an inverted density

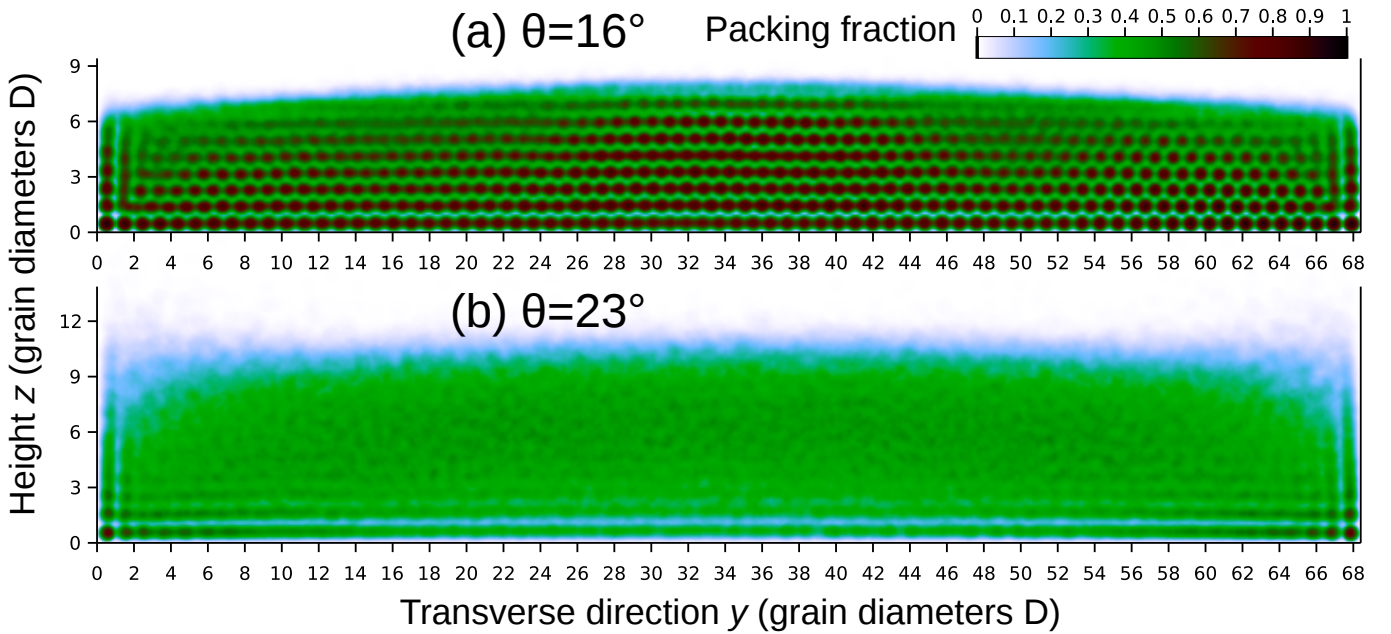


Figure 7. (Color online). Packing fraction map, averaged over x . The layered structure at low angles disappears when granular convection takes place.

θ	14°	15°	16°	17°	18°	19°	20°	21°	22°	23°
$\widehat{\mu_W}$	0.27	0.28	0.31	0.32	0.35	0.36	0.36	0.37	0.38	0.38

Table II. Global effective friction coefficient on the wall (to compare with the microscopic $\mu_{gw} = 0.596$).

profile (Fig. 6), similar to these reported in the literature for bumpy boundaries [10, 13], while the layer in contact with the flat boundaries remains clearly separated (Fig. 6 and 7b).

B. Pressure and effective friction

We did not implement a full calculation of the stress tensor, but stresses on the boundaries are easily deduced from the forces exerted by the grains during each contact, averaged over a $500\sqrt{D/g}$ time window. Let us denote by $\mathbf{f}^{g \rightarrow w}(z)$ the stress vector exerted on one wall, at height z , by the grains. The force exerted by one wall on the grain flow is simply: $\mathbf{F}^{w \rightarrow g} = - \int_{x=0}^L \int_{z=0}^{\infty} \mathbf{f}^{g \rightarrow w}(z) dx dz = L \int_{z=0}^{\infty} \mathbf{f}^{w \rightarrow g}(z) dz$. Using the subscript n and t to distinguish the normal and the tangential components, the local effective friction coefficient on the wall is then computed as $\mu_w(z) = \|\mathbf{f}_t(z)\| / \|\mathbf{f}_n(z)\|$. The global effective friction coefficient is computed as $\widehat{\mu_W} = \|\mathbf{F}_t\| / \|\mathbf{F}_n\|$. The profiles in z and the values of the effective friction on the walls are shown in Fig. 9 and Table II. The observed friction weakens with depth and is similar to that reported in [42].

Let us consider a slab at the top of the flow (from z and above) as a continuum.

\mathbf{F}_m = weight
 $\mathbf{F}_n^w, \mathbf{F}_n^b$ = normal reaction of the wall / base
 $\mathbf{F}_t^w, \mathbf{F}_t^b$ = tangential reaction of the wall / base

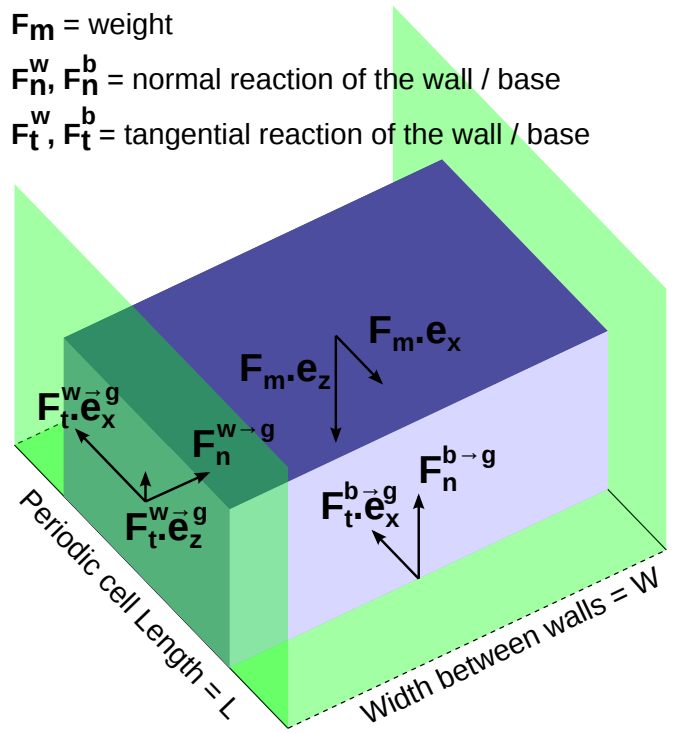


Figure 8. (Color online). External forces balance on the grain flow.

The balance of external forces along z implies: $\left(\int_{x=0}^L \int_{y=0}^W \int_z^{\infty} \nu(x, y, z') dx dy dz' \right) \rho g \cos \theta = P(z) LW + 2L \int_z^{\infty} \mathbf{f}_t^{w \rightarrow g}(z').\mathbf{e}_z dz'$ with $P(z)$ the average pressure on an xy plane section computed at height z .

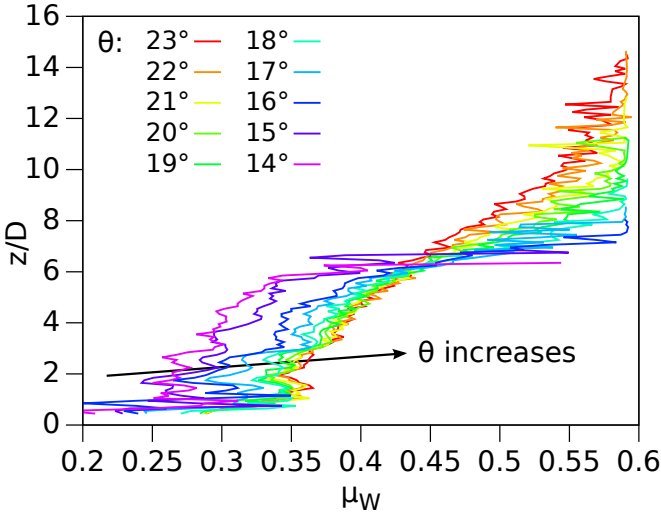


Figure 9. (Color online). Friction coefficient profile on the lateral walls for several value of the inclination angle θ .

The contribution of the walls to this balance is always very small compared to the other terms (of the order of one per cent). The vertical profiles of $P(z)$ are shown in Fig. 10 for each angle θ , normalized so the value at the base equates the mass holdup \tilde{H} we use. They are linear over the most part, except for the basal rolling layer and the very diluted top consisting of a few grains in ballistic motion. Thus, over the main bulk of the flow, the approximation $P(z) \approx (H_p - z) \bar{\nu} \rho_g g \cos \theta$ is excellent (with $\bar{\nu}$ the average packing fraction on the bulk). The corresponding effective flow heights H_p are shown in Fig. 10 (inset). They confirm the general dilation of the flow with the angle θ , matching the general packing fraction decrease of Fig. 6. The total frictional influence of the walls on the flow can also be quantified. The ratio between the weight of the grains and the friction force on the walls: $\bar{\mu}_w H_p / W$ [22, 43] is at most 0.06 for $\theta = 23^\circ$. This justifies the arguments developed in [2] and used here for neglecting the friction on the walls, for a shallow flow with a large width.

The pressure at any position on the flat base $P_B(y) = \mathbf{f}_n^{g \rightarrow b}(y) \cdot \mathbf{e}_z$ is shown in Fig. 11, normalized so the average value is the mass holdup $\tilde{H} = 4$. In the unidirectional regimes grains do not deviate much in y from their trajectories along x , leading to large pressure fluctuations on the base. In the convective regime, the grain circulation due to the secondary flows smooth out these differences. In each case pressure is maximal at the center of the flow, and decreases in the lateral parts near the walls.

C. Mean velocity and fluctuations

A continuous mean velocity field $\bar{\mathbf{v}}$ is computed using the definition by Serero et al. [44] for polydisperse systems, and averaged over time:

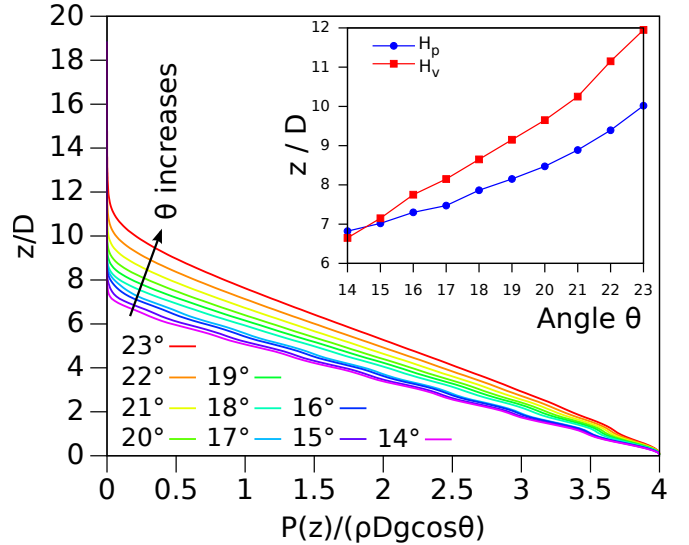


Figure 10. (Color online). Main diagram: Vertical profiles of the averaged pressure for the hydrostatic approximation in the center part of the curves. Inset: The effective heights of the flows, with respect to the hydrostatic approximation H_p and maximal flow velocity H_v . See the main text.

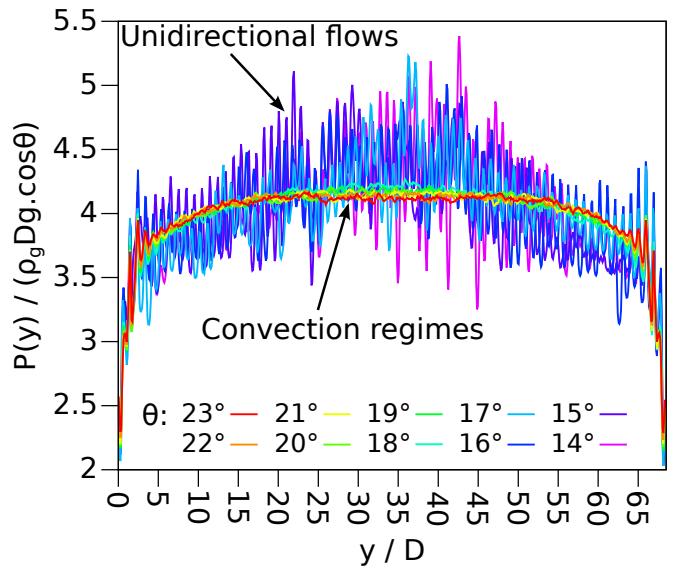


Figure 11. (Color online). Normalized pressure computed from each contact with the base, smoothed over $\pm 1D$ in y

$\bar{\mathbf{v}}(\mathbf{x}) = \left\langle \sum_{i=1}^N \mathbf{v}_i k_i(\mathbf{x}_i - \mathbf{x}) \right\rangle_\tau / \left\langle \sum_{j=1}^N k_j(\mathbf{x}_j - \mathbf{x}) \right\rangle_\tau$, where $\mathbf{x} = (x, y, z)$ is the 3D position at which to compute the average velocity, \mathbf{x}_i is the position of the center of grain i , and k_i is a kernel that distributes the mass m_i of grain i over space. We use the uniform density kernel $k_i(\mathbf{x}_i - \mathbf{x}) = \rho$ when $\|\mathbf{x}_i - \mathbf{x}\| < r_i$ with r_i the radius of grain i , and 0 elsewhere. We then define a “granular temperature” [44] from the velocity fluctuations: $T = \frac{1}{2} (\|\mathbf{v}\|^2 - \|\bar{\mathbf{v}}\|^2)$ where the overline denotes the above weighted averaging.

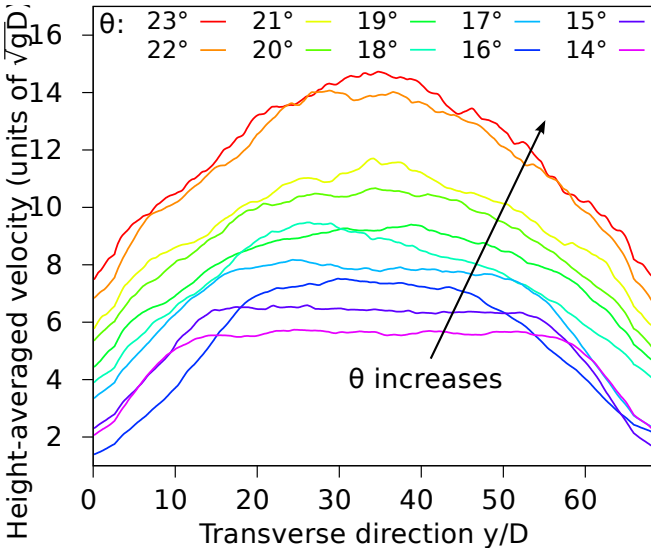


Figure 12. (Color online). Transverse velocity profile, smoothed over $\pm 2.5D$ in Y , averaged over z .

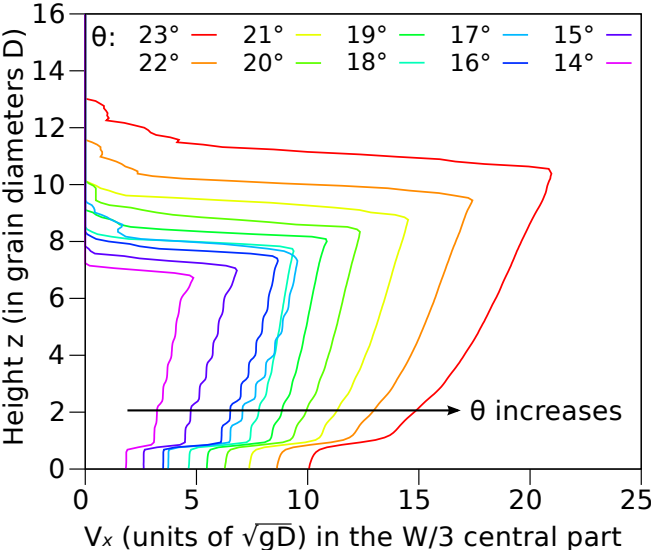
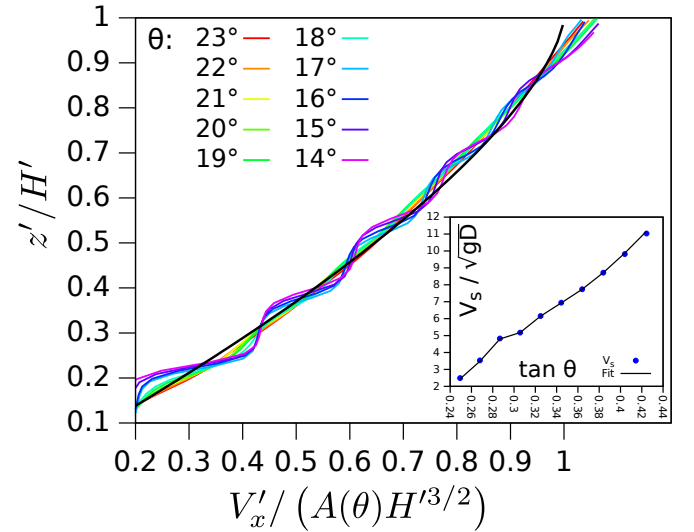


Figure 13. (Color online). Height profile of the velocity along x averaged over the central part of the flow.

For the unidirectional flows Fig. 12 reproduces the experimental mean velocity transverse profile (Fig. 1), where the shearing layer induced by the walls extends to about $1/3$ within the flow. The shape of the velocity profile in the unidirectional regime, considering the average packing fraction is constant in z (Fig. 6), is comparable to the experimental measures in Fig. 3 (4) of [28] at similar angles. Within the central part we obtain velocity profiles (Fig. 13) similar to these given by PBC [31]. The velocity reaches a maximal value at height H_v then decreases rapidly in the sparse ballistic layer of grains. The values of H_v can be compared to H_p in the inset of Fig. 10. The 3D velocity profile of the flow can be inferred from Figs. 12 and 13 as a faster region in the



center part, sheared vertically, on top of a basal rolling layer of grains. The transverse velocity profile (Fig. 12) is sheared through the whole width in the presence of secondary rolls. These convey grains up to the center of the flow, as seen in Fig. 17.

The basal layer of rolling and bumping grains can be interpreted as an effective base for the main bulk of the flow on top of it. A sliding velocity V_s can be defined as the velocity in the direction of flow at $z_0 = 1.5D$, corresponding to the mean velocity of the grains in the second layer, just above the basal grains. Now, let $V'_x = (V_x - V_s)/\sqrt{gD}$, $z' = (z - z_0)/D$, and $H' = (H_p - z_0)/D$. Bagnold’s constitutive equation [12] states that the pressure $P(z)$ relates to the shear rate with $\frac{\partial V'_x}{\partial z'} \propto \sqrt{P(z')}$. Integrating this relation and assuming that it holds in a reference frame moving with velocity V_s , we shall have $V'_x = A(\theta) \times (H'^{3/2} - (H' - z')^{3/2})$, with $A(\theta)$ a constant that is related to the inertial number defined in the next section. Fig. 14 shows that this is indeed the case, that all the vertical profiles of the velocity indeed collapse on the theoretical curve above the rolling layer. The “sliding velocities” V_s are shown in inset of Fig. 14, with an excellent fit between the measured V_s at $z_0 = 1.5D$ and the fitted value from the Bagnold profile. V_s increase roughly linearly with $\tan \theta$.

Globally, flows on flat frictional surfaces can thus be decomposed into a rolling basal layer, above which the main bulk of the flow follows the classical Bagnold scaling. This is consistent with the observations reported in [1, 3]. Note that, as we have averaged over the transverse direction, this analysis however tells nothing on the internal flow structure visible in the previous sections.

Fig. 17 shows the color-coded map of the “granular temperature” T in the cross-section yz plane. Height profiles of T , averaged on the whole width for each z ,

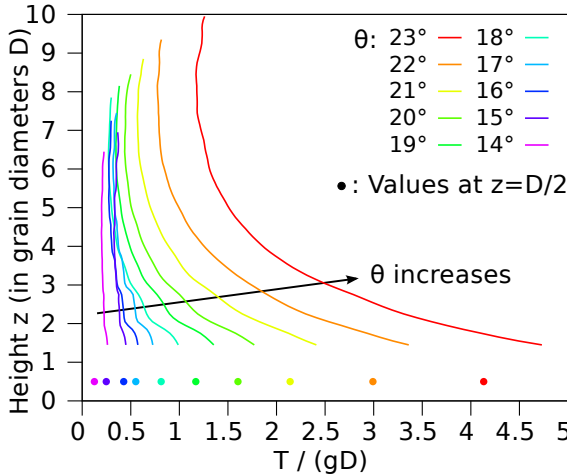


Figure 15. (Color online). Vertical profile of the velocity fluctuations, averaged over y .

are shown in Fig. 15, computed in the bulk of the flow above $z_0 = 1.5D$. The strong velocity gradient at the transition between the bulk and the basal rolling layer (see Fig. 13) prevents a meaningful computation of T in that transition. Fig. 15 also shows as separate points the basal “temperature” value that takes into account only contributions from the rolling layer. The main bulk of the flow thus rests on top of an effective base with higher “granular temperature” and large gradient, which then decreases according to a height profile compatible with those found in the core flow on bumpy bases, in numerical simulations [12] of thick flows. In these simulations [12], the influence of a bumpy base extends to $z = 5D$ at which point the “granular temperature” is maximal (Fig. 6 of [12]), and then it decreases with the height. Note that the temperature profiles reported in Fig. 15 are also compatible with those predicted by the kinetic theory [13, 30] and with the early 2D simulation results in [25].

The granular temperature T is nearly constant over the bulk (Fig. 15) in the unidirectional regime. In the convective regime, Fig. 17 shows a z profile inversion between the values at walls and the center that resembles Figs. 15a and 15b of [33], where similar profiles were computed on a bumpy base with flat frictional walls. The highest temperatures occur near the center of the base (Fig. 16), the temperature gradient is large near the side walls (at least at the base). All these features are thus coherent with the idea of a basal layer producing an effective bumpy base.

D. Analogy with Rayleigh-Bénard convection

Matching experimental evidence for secondary flows was first seen in [11], on a bumpy base. Spontaneous generation of longitudinal vortices in rapid granular flows

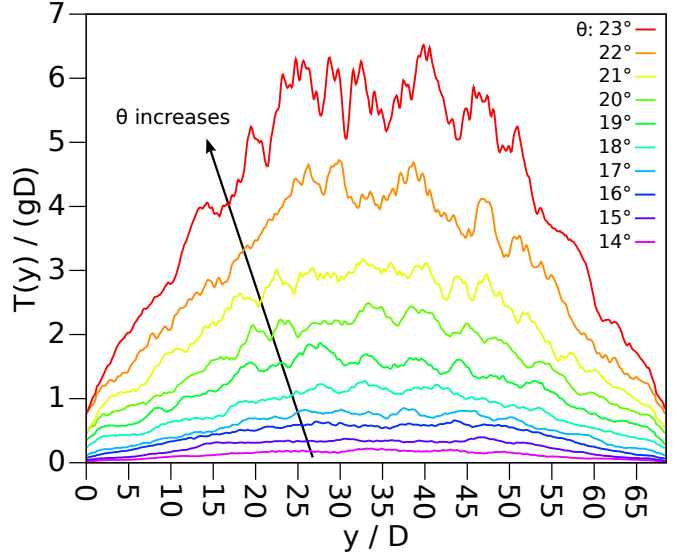


Figure 16. (Color online). Transverse profile of the velocity fluctuations at the flat base, smoothed over $\pm 2.5D$ in y .

down rough inclined planes are also been reported in [19]. The dense and faster troughs correspond to the downward part of the flow, while the dilute and slower crest correspond to the upward part. In order to explain them an analogy with Rayleigh-Bénard convection was proposed [13] for granular flows based on considerations from the kinetic theory for granular gases [6]. A three-dimensional linear stability analysis of SFD flows reveals that in a wide range of parameters, they are unstable under transverse perturbations. The structure of the unstable modes is globally in good agreement with the rolls we observe in the main plug of our flows on a flat base, despite packing fractions reaching high values $\nu_{max} > 0.4$ in the core in our case (see Fig. 6), unlike the experiments on a rough base reported in [13] where $\nu_{max} \approx 0.2$. These values of ν_{max} are similar to those obtained in the numerical simulations of [10]. In [10] two different regimes of stripes are described, but the granular temperature is not available. The “dilute” regime corresponds to the regime described in [13, 19] where the dense fast region with downwards motion corresponds to a height minimum, while in the “dense” regime it corresponds to a height maximum. The dense regime is observed for an average packing fraction $\bar{\nu}$ comprised between 0.36 and 0.57, while $0.12 < \bar{\nu} < 0.42$ in the dilute regime. It is difficult in our case to know which regime correspond our rolls correspond to. The average density is in the common range, and the curvature of the surface is not a clear indication as the walls could deform it.

Fig. 17 shows the color-coded map of T and the velocity field in the cross-section yz plane. We can see that the motion in the bulk part of the transverse plane consists of a pair of counter-rotating vortices - The Fig. 5b in [11] shows a similar roll orientation. The material moving towards the base, in the central part is flowing faster in x

Arrows: Mean velocity in the YZ plane
 Color: Temperature
 From top to bottom: $\theta = 17^\circ, 20^\circ, 23^\circ$

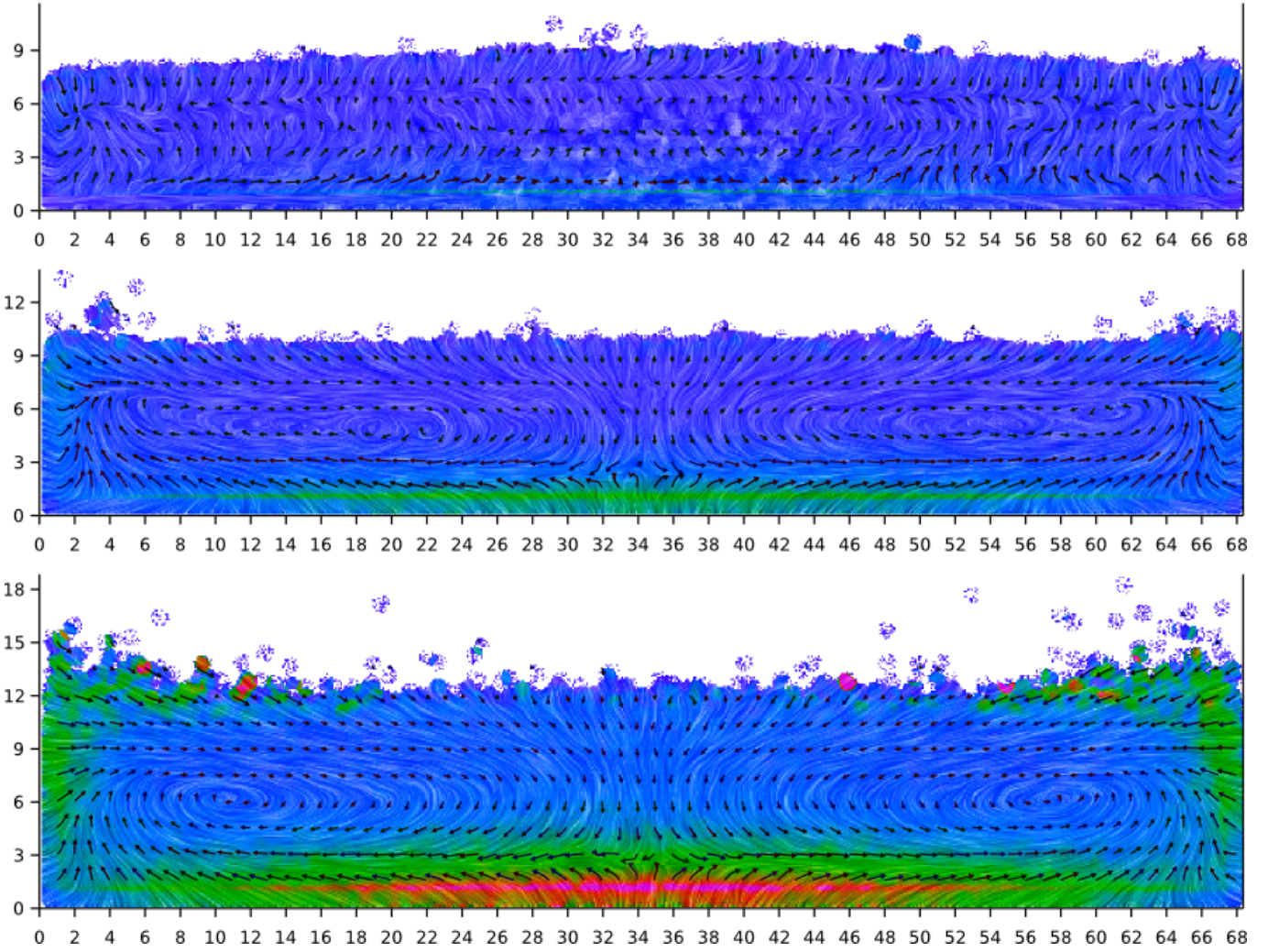
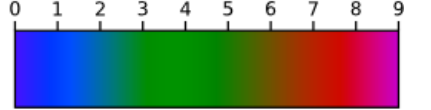


Figure 17. (Color online). Vector field of the velocities in the transverse yz plane on top of the color/gray-coded “granular temperature” T . The data, obtained in the steady and fully developed regime, have been averaged over time and over the periodic cell in the direction of the flow.

direction than the grains rising up on the sides. The average density is higher where the flow is downwards and smaller where the flow is upwards. We also observe the temperature vertical profile inversion reported in Fig. 8d of [13]: the temperature gradient is opposed to the transverse velocity in the downward and upward parts of the vortices.

Interestingly, the Rayleigh-Bénard regime is similar to the convection that occurs when a granular bed on a bumpy base is shaken at high intensity [45]. In such a system the shaking and the bumpiness of the base lead to a higher granular temperature in the vicinity of the base. The granular bed is then heated from below and cooled

from above. In our system, as shown above, the granular layer in contact with the flat frictional base can be considered as a bumpy sliding base atop which a sheared flow occurs.

VI. VISCOPLASTIC RHEOLOGY

A viscoplastic rheology for incompressible flows was proposed in [7], as a 3D extension of the proposal in [4]. We expect it to hold in the unidirectional flows case, for which [4] was proposed. In [10], Börzsönyi *et al.* have shown that the viscoplastic rheology does not hold lo-

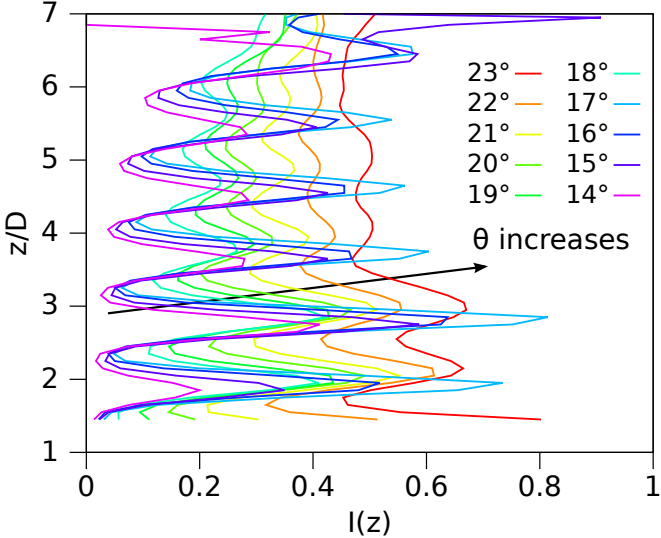


Figure 18. (Color online). Vertical profile of the inertial number I .

cally for granular convection in the bumpy boundaries case. They then propose an extension for this rheology to compressible flows.

This section investigates the situation for the flat frictional scenario, with an effective basal layer, together with a form of the rheology using averaged quantities for a global analysis. We average the constitutive equation proposed in [7] to match the vertical profile of $P(z)$ presented in the previous section, leading to the definition of an inertial number $I(z) = |\langle \dot{\gamma} \rangle(z)| D / \sqrt{P(z)/\rho_g}$. In this expression the strain rate tensor $\dot{\gamma}$ is averaged at each z location over L and W , $\langle \dot{\gamma} \rangle(z) = \frac{1}{LW} \int_{x=0}^L \int_{y=0}^W \dot{\gamma} dx dy$, and the norm used is the same as in [7] (i.e. $|a| = \sqrt{\frac{1}{2} \sum_{i,j} a_{ij}^2}$), which recovers the 1D expression of I from [4] when the $\dot{\gamma}$ tensor is strongly dominated by $\frac{\partial v_x}{\partial z}$). We use the definition of I from [7] in which the grain density ρ_g is used for normalization, while the original proposal [4] used the density of the continuum $\rho_c = \rho_g \bar{\nu}$. Literature on this topic shows that both approaches are in use (e.g. [24, 46] use ρ_g , [10] use ρ_c). The averaging we propose cancels the transverse v_y and vertical v_z velocity components thanks to the symmetry of the inner rolls (see Fig. 17), recovering an expression that effectively behaves as for a unidirectional flow without internal structure. Moreover, we checked that the norm of $\langle \dot{\gamma} \rangle(z)$ differs from the norm of its deviator by less than 0.35%, hence the condition for an incompressible flow is satisfied on average (i.e. local dilations that may occur along y in the rolls, if any, cancel in any given z slice). In these conditions, we expect the constitutive equation using the average $\langle I \rangle$ to hold quite well, which is indeed the case (see below).

Fig. 18 shows the vertical profile of $I(z)$. Above the basal layer the average $\langle I(z) \rangle_{6.5 > z/D > z_0/D = 1.5}$ is defined in the main bulk of the flow. Oscillations over that av-

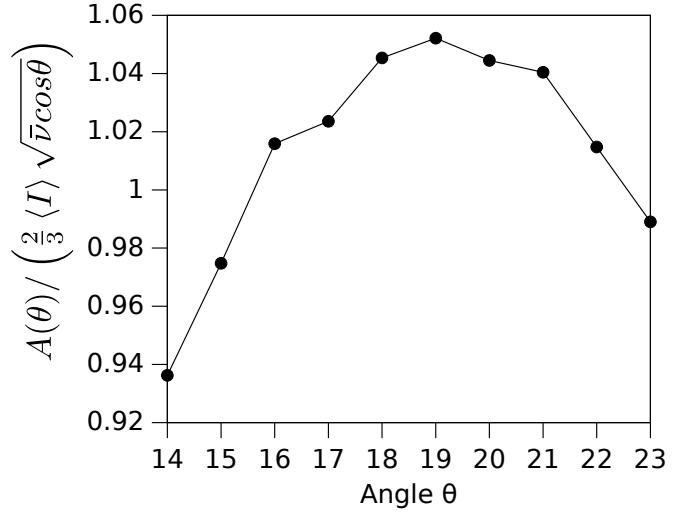


Figure 19. Fit quality of the theoretical Bagnold profile for each angle.

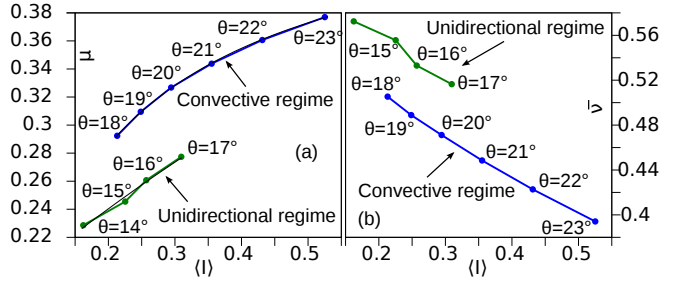


Figure 20. (Color online). (a) Effective friction μ and (b) average packing fraction $\bar{\nu}$ vs average inertial number $\langle I \rangle$ in the bulk of the flow. Overlaid thin black lines in (a) are the empirical fits mentioned in the main text.

eraged value are present in the unidirectional regimes, matching the layered structure previously mentioned in Section V A, while for the convective regimes the vertical profile does not vary as much $I(z) \approx \langle I \rangle$. Note that for the dense flows on bumpy base case, I is assumed to be constant on the whole height (Section 8.4.1 of [4]).

If the constitutive equation of [7] holds in the averaged form we propose, we shall recover a velocity profile in the form of a Bagnold scaling (eq. 25 of [4]), with $A(\theta) = \frac{2}{3} \langle I \rangle \sqrt{\bar{\nu} \cos \theta}$ matching the constant fitted in the previous section. Fig. 19 shows that this is indeed the case, up to a worst-case 5% accuracy.

From the momentum balance for the main bulk flowing on the basal layer, including wall effects, it is possible to obtain $\mu(\langle I \rangle)$, the effective friction coefficient of the main bulk on the basal layer: $\mu = \tan(\theta) - \widehat{\mu_W} (H_p - z_0) / W$ [22, 24]. When $\langle I \rangle$ is plotted against $\mu(\langle I \rangle)$ the separation between the unidirectional and the convective regimes is clearly apparent as a discontinuity, see Fig. 20a. The best fit parameters for the constitutive equation $\mu(\langle I \rangle) = \mu_s + (\mu_2 - \mu_s) / (1 + I_0 / \langle I \rangle)$ proposed in [7] (see Fig. 20a) are $\mu_s = 0.0046$, $\mu_2 = 0.479$ and $I_0 = 0.13$

in the convective regime, while $\mu_s = 0.16$, $\mu_2 = 1.02$ and $I_0 = 2.06$ in the unidirectional regime, showing that the empirical constitutive equation $\mu(\langle I \rangle)$ changes during the transition. The break is similarly visible on the $\bar{\nu}$ vs $\langle I \rangle$ profile in Fig. 20b. Both branches decrease nearly linearly, compatible with Fig. 2 in [46] where the model coefficient of restitution and spring stiffness are varied in a 2D simulation, and unlike Fig. 4e of [10] where the $\bar{\nu}(I)$ relation is built locally and not in averaged form.

The number I can also be interpreted as the ratio of a macroscopic rearrangement time scale over a shearing time scale [4]. The observed drastic reduction in I at the transition between the unidirectional and convective regimes reflects the fact that granular convection rearranges the grains much faster than slow diffusion within the ordered layering. The $\langle I \rangle$ value at $\theta = 18^\circ$ in Fig. 20 is consistent with the convective regime despite computations being performed in the oscillating state, leading to the hypothesis that the oscillations are related to the onset of convection. That hypothesis will be investigated in a future work.

VII. CONCLUSION

Our numerical simulations with side walls generate SFD flows comparable to the experimental setup [2] with a compatible range of angles, distances of establishment and velocity profiles. We confirm that the influence of the friction on the lateral walls is negligible ([2] and Section VI), but also that walls manifest in other ways a long-range influence within the flow ([2] and Fig. 12). In any case, side walls cannot be ignored even when they are far away, especially since channeled flows can be directly compared to experiments. Building on these results we extrapolate the simulation to larger inclination angles

and find that distances for reaching the steady states exceed the experimental chute length. These regimes also correspond to the presence of granular convection, whereby grains are circulated within the whole flow, unlike the unidirectional regimes where grains mostly remain in a “crystallized” layered structure.

Compared to the well-studied bumpy base scenario, flows on flat frictional surfaces involve a much faster overall velocity, thanks to the presence of a basal layer of rolling grains, upon which slides the main bulk of the flow. We then interpret that bottommost layer of grains as an effective base for the flow bulk and we show that in these conditions, the bulk follows a conventional Bagnold scaling. The analogy with an effective rough base extends to the presence of a convective regime with similar velocity and density profiles. However, due to the increased overall velocity, and owing to the effective base being less rigid than a fixed bumpy one, the convection rolls appear for lower angles and mass holdups in the flat frictional case than in the bumpy one.

As for the bumpy case, we find that over the effective base the bulk of the flow follows on average a viscoplastic rheology [7], for each of the SFD regimes. The transition between these regimes corresponds to a break in the friction μ versus inertial number I relation (Fig. 20), with a drastic reduction in I that matches the effect of the secondary rolls (faster grain rearrangement).

Channeled flows down flat frictional surfaces are well adapted for testing granular rheologies numerically and studying boundary conditions.

Acknowledgments We thank Région Bretagne for funding (CREATE Sampleo Grant), M.Y.Louge, and J.T.Jenkins for helpful discussions and comments. We are grateful to Sean McNamara for a careful reading of the manuscript.

- [1] R. Delannay, M. Louge, P. Richard, N. Taberlet, and A. Valance, Nat. Mat. **6**, 99 (2007).
- [2] M. Y. Louge and S. C. Keast, Phys. Fluids **13**(5), 1213 (2001).
- [3] N. Taberlet, *Écoulements gravitaires de matériaux granulaires*, Ph.D. thesis, Université de Rennes 1 (2005).
- [4] GDR-MiDi, Eur. Phys. J. E **14**, 341 (2004).
- [5] R. Nedderman and C. Laohakul, Powder Tech. **25**, 91 (1980).
- [6] J. T. Jenkins and S. B. Savage, J. Fluid Mech. **130**, 187 (1983).
- [7] P. Jop, Y. Forterre, and O. Pouliquen, Nature **441**, 727 (2006).
- [8] O. Pouliquen, Phys. of Fluids **11**, 542 (1999).
- [9] J. Jenkins and D. Berzi, Gran. Mat. **12**, 151 (2010), 10.1007/s10035-010-0169-8.
- [10] T. Börzsönyi, R. E. Ecke, and J. N. McElwaine, Phys. Rev. Lett. **103**, 178302 (2009).
- [11] S. B. Savage, J. Fluid Mech. **92**, 53 (1979).
- [12] L. E. Silbert, D. Ertas, G. S. Grest, T. C. Halsey, D. Levine, and S. J. Plimpton, Phys. Rev. E **64**, 051302 (2001).
- [13] Y. Forterre and O. Pouliquen, J. Fluid Mech. **467**, 361 (2002).
- [14] W. Bi, R. Delannay, P. Richard, and A. Valance, Phys. Fluids **18**, 123302 (2006).
- [15] E. Azanza, *Écoulements granulaires bidimensionnels sur un plan incliné*, Ph.D. thesis, École des ponts et chaussées, Marne la Vallée, France (1997).
- [16] G. Berton, R. Delannay, P. Richard, N. Taberlet, and A. Valance, Phys. Rev. E **68**, 051303 (2003).
- [17] S. Dippel, *Microscopic dynamics of granular materials*, Ph.D. thesis, High Performance Computing Center, Stuttgart (1998).
- [18] N. Taberlet, P. Richard, J. T. Jenkins, and R. Delannay, Euro. Phys. J. E: Soft Mat. Bio. Phys. **22** (2007), 10.1140/epje/e2007-00010-5.
- [19] Y. Forterre and O. Pouliquen, Phys. Rev. Lett. **86**, 5886 (2001).

- [20] L. E. Silbert, G. S. Grest, S. J. Plimpton, and D. Levine, Phys. Fluids **14**, 2637 (2002).
- [21] C. Ancey, Phys. Rev. E **65**, 011304 (2001).
- [22] N. Taberlet, P. Richard, A. Valance, W. Losert, J. M. Pasini, J. T. Jenkins, and R. Delannay, Phys. Rev. Lett. **91**, 264301 (2003).
- [23] W. Bi, R. Delannay, P. Richard, N. Taberlet, and A. Valance, J. Phys.: Cond. Matt. **17**, S2457 (2005).
- [24] P. Jop, Y. Forterre, and O. Pouliquen, J. Fluid Mech. **541**, 167 (2005).
- [25] C. S. Campbell and C. E. Brennen, J. Appl. Mech. **52**, 172 (1985).
- [26] C. S. Campbell, C. E. Brennen, and R. H. Sabersky, Powder Tech. **41**, 77 (1985).
- [27] J. S. Patton, C. E. Brennen, and R. H. Sabersky, J. Appl. Mech. **54**, 801 (1987).
- [28] P. C. Johnson, P. Nott, and R. Jackson, J. Fluid Mech. **210**, 510 (1990).
- [29] H. Ahn, C. E. Brennen, and R. H. Sabersky, J. Appl. Mech. **58**, 792 (1991).
- [30] H. Ahn, C. E. Brennen, and R. H. Sabersky, J. Appl. Mech. **59**, 109 (1992).
- [31] O. R. Walton, Mech. Mat. **16**, 239 (1993).
- [32] M. Sadjadpour and C. S. Campbell, Adv. Powder Tech. **10**, 175 (1999).
- [33] D. M. Hanes and O. R. Walton, Powder Tech. **109**, 133 (2000).
- [34] A. Lorenz, C. Tuozzolo, and M. Y. Louge, Exp. Mech. **37**, 292 (1997).
- [35] P. Cundall and O. Strack, Géotechnique **29**, 47 (1979).
- [36] S. Luding, Eur. J. Env. Civil Eng. **12**, 785 (2008).
- [37] H. Kruggel-Emden, S. Wirtz, and V. Scherer, Chem. Eng. Sci. **63**, 1523 (2008).
- [38] L. Pournin, T. M. Liebling, and A. Mocellin, Phys. Rev. E **65**, 011302 (2001).
- [39] A. D. Renzo and F. P. D. Maio, Chem. Eng. Sci. **59**, 525 (2004).
- [40] H. Kruggel-Emden, E. Simsek, S. Rickelt, S. Wirtz, and V. Scherer, Powder Tech. **171**, 157 (2007).
- [41] P. Richard, S. McNamara, and M. Tankeo, Phys. Rev. E **85**, 010301(R) (2012), submitted.
- [42] P. Richard, A. Valance, J.-F. Métayer, P. Sanchez, J. Crassous, M. Louge, and R. Delannay, Phys. Rev. Lett. **101**, 248002 (2008).
- [43] N. Taberlet, P. Richard, R. Delannay, and M. Y. Louge, in *Powders and Grains* (H.Herrmann, G. Gudehus, S. Luding, & K. Sommer (eds), A. Balkema, NY, 2005) pp. 873–876.
- [44] D. Serero, C. Goldenberg, S. H. Noskowicz, and I. Goldhirsch, Powder Tech. **182**, 257 (2008).
- [45] P. Eshuis, D. van der Meer, M. Alam, H. J. van Gerner, K. van der Weele, and D. Lohse, Phys. Rev. Lett. **104**, 038001 (2010).
- [46] F. da Cruz, S. Emam, M. Prochnow, J.-N. Roux, and F. Chevoir, Phys. Rev. E **72**, 021309 (2005).